

# An Objective Measure for Automotive Surface Contamination

## Abstract

Surface contamination, or soiling, of the exterior of road vehicles can be unsightly, reduce visibility and customer satisfaction and, with the increasing application of surface mounted sensors, can degrade the performance of advanced driver assistance systems. Experimental methods of evaluating surface contamination are increasingly used in the product development process, but the results are generally subjective. The use of computational methods for predicting contamination make objective measures possible, but comparable data from experiment is an important validation requirement.

This paper describes the development of an objective measure of surface contamination arising during experiments. A series of controlled experiments using Ultra Violet (UV) dye doped water are conducted to develop a robust methodology. This process is then applied to a simplified contamination test. An image of a surface, illuminated by an UV lamp, is captured after every test along with a calibration vessel with known fluid depth. The image is processed to remove the influence of variation in incident illumination. The total mass of contamination deposited is then calculated using the calibration vessel to provide the required local fluid depths. The paper includes validation of the technique.

## Introduction

Surface contamination, whether dry or wet, is an issue for all automotive manufacturers. Hagemeyer *et al.* [1] neatly distills the work of Kuthada *et al.* [2] by describing three sources of contamination; Primary sources are a direct result of rain, third-party (or foreign) sources are generated by dirt or splash and spray from other vehicles and self-soiling refers to the contamination caused by the vehicle itself, for example generated from the wheels and tyres. The contamination can affect many areas of the vehicle but is often most noticeable on the base where flow recirculation in the wake tends to transfer contamination onto the base. This base contamination is of particular importance to two-box geometries, such as SUVs [3]. In addition to being unsightly, contamination can create problems for the driver such as:

- Reduced visibility through the rear screen.
- Degraded performance of advanced driver assistance systems by reducing the effectiveness of cameras, sensors and lights that may be placed on the base.
- Contamination being transferred to skin and clothing when accessing the boot (trunk).

Hagemeyer *et al.* [1] provides a thorough review of front and side-glass surface contamination both experimental and numerical.

Gaylard *et al.* [4] takes this a stage further with a complete review of all surfaces both experimentally and numerically. Neither review, however, identifies a reliable and truly objective method of measuring surface contamination experimentally. More typically the work reported provides only subjective comparisons between experimentally generated and simulated contamination. At best a relative measure of soiling, or degree of soiling, is defined [5]. Using an image taken from a soiling experiment the number of pixels that show contamination are divided by the total number of pixels for a region of interest as shown in Equation 1.

$$VG = \frac{\sum_{n=0}^N P(n)|_{contaminated}}{N} \quad (1)$$

While this results in a number that can be used for comparisons it is based on a simple binary value; there is either contamination or there isn't. As such, no distinction can be made between a pixel that has a very small volume of fluid on it and one that is part of a thin film.

Gaylard *et al.* [7] for example, compares wind tunnel tests, on-road tests and simulations. The wind tunnel experiment employs water doped with a UV tracer and the image generated is processed to provide intensity (Figure 1). The on road tests were performed on wetted gravel (Figure 2).

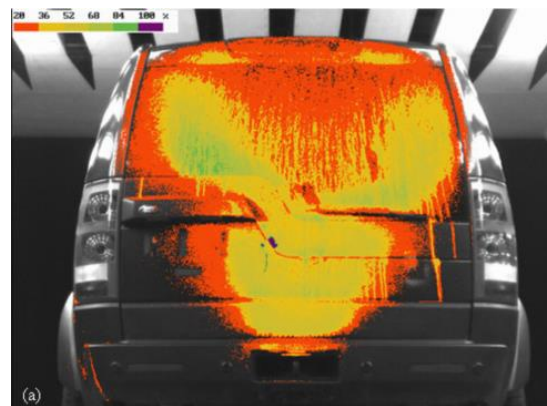


Figure 1. Deposition intensity analysis for a SUV in a wind tunnel test using UV illumination with doped water [7]

The image from the wind tunnel test is useful for identifying areas of relatively higher and lower contamination, but the image also clearly shows the formation of rivulets, especially in the centre and on the right hand side of the base. The rivulets obscure the data somewhat as they move the doped water from the impact point, thus erasing the correct location data. This suggests that in this case the test was run

beyond the saturation point. Equally, the on road test, Figure 2, shows that virtually the entire base is dirty, making it impossible to draw any objective conclusions from such a test other than the limits of wet contamination for a test of this (unspecified) duration. As was noted by Gaylard *et al.* [7] the uncontrollable environmental conditions will have an impact on the contamination rate and pattern. Equally, the fact that the track is a circuit will bias the final contamination. These factors suggest that test tracks are not ideal for obtaining contamination data for comparative studies.



Figure 2. Deposition image for a SUV from a wetted gravel test track [7]

Jilesen *et al.* [8] employed the same experimental test data with an improved simulation process that included a time history of the volume of water on the base. To improve the experimental approach Gaylard *et al.* [6] conducted further controlled experimental testing at full scale on a SUV. Doped water is injected across the front of the contact patch on the rolling road at a known rate and the base is illuminated. Images are captured and the intensity then compared with simulated data. The approach ensured a more realistic soiling mechanism, but the final comparisons still rely on relative or subjective data.

In addition to the studies of base soiling, contamination of the vehicle side is also reported in a number of studies [7, 8, 9]. Karbon and Longman [9] visually compares some early CFD work to still images of water flowing around an A-pillar from the windscreen and on to the side glass. The successful comparison between a configuration tested in both experiment and simulation then allows geometry modifications to be tested in simulation.

To improve the ability to compare experiments and computational contamination Kabanovs *et al.* [10,11] report on tests on quarter-scale simplified automotive geometries using a UV dye to dope water injected as a spray behind the left hand rear wheel. Using a single injection point was designed to assist understanding of the final result. After running for a fixed period the base was illuminated with UV light and the image processed to provide intensities. Figure 3 shows an example grayscale image following a test, where grayscale is a range of intensities in the image. A calibration vessel can be seen to the left of the model.

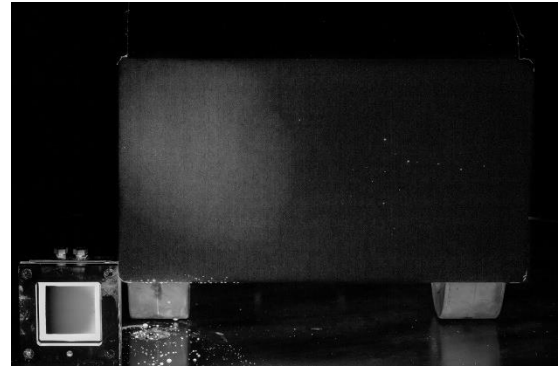


Figure 3. Example contamination from quarter scale testing of a generic SUV [11]

To ensure full comparability between experimental and computational work Kabanovs uses the full experimental setup in the simulation, including the wind tunnel geometry and the measured spray inlet velocity and droplet distribution. However, the subsequent comparison is ultimately limited because the experiment provides only a qualitative image whereas the simulations produce numerical outputs that can be used for comparison, including a time history of deposited mass. It is notable that the simulations reported by Kabanovs use detailed experimental data including base pressures PIV and balance to validate the aerodynamic flow-field. Similar, high quality objective data to compare contamination regions are not however available. But, the advantage of developing sophisticated CFD simulations that can be used to explain how the contamination occurs and the precise source of each area of contamination is clear.

The experimental approaches described in the preceding sections all use a similar underlying approach; employing UV doped water, image processing to generate intensity and a subjective evaluation based on the premise that intensity is linearly proportional to fluid depth. While in practice the image will be affected by spatial variations in incident illumination intensity that is not considered in the literature it is understood that efforts are taken in their application. In addition, the intensity of the emitted light captured in the image is not linearly proportional to the mass of fluid, or depth of contamination, that has been deposited.

To obtain a measure of deposited film Aguinaga *et al.* [12] performs an experiment using doped water as a UV reactive source and describes a calibration method using five known depths of fluid to provide relevant average intensities for a curve fit. The depths are described as being calibrated though details on how this was achieved are not included. It is assumed, as with Hagemeyer's similar work [13], that the incident intensity is uniform. Aguinaga validates the process against droplets created with a pipette to within 10 % of the target volume; no estimates on the accuracy of the droplet generation are given. Aguinaga's experiment is to determine the deposition thickness in an axisymmetric suddenly expanding flow, so while not an automotive problem the treatment provides a useful starting point.

Aguinaga's derivation, repeated below, details the relationship between the incident intensity  $I_o$ , emitted intensity  $I_f$ , fluid depth  $x$  and the recorded camera grayscale  $g_t$ . The Beer-Lambert law relates the thickness of fluid to the absorbance  $A_\lambda$  for a given wavelength as shown in Equation (2):

$$A_\lambda = \log\left(\frac{I_o}{I_f}\right) \quad (2)$$

Where  $I_t$  is the transmitted intensity through the fluid. The absorbance can also be given by Equation (3):

$$A_\lambda = C_{UV} \cdot x \cdot \varepsilon_\lambda \quad (3)$$

Where  $C_{UV}$  is the dye concentration and  $\varepsilon_\lambda$  is the molar absorbption of the dye at wavelength  $\lambda$ . Substituting Equation (3) into Equation (2) and modelling the emitted intensity,  $I_f$ , through a linear relationship with transmitted intensity gives Equation (4):

$$I_f = \Phi \cdot I_o \cdot (1 - e^{-C_{UV} \cdot x \cdot \varepsilon_\lambda}) \quad (4)$$

Where  $\Phi$  is the quantum efficiency of the dye (the ratio of energy emitted to energy absorbed). If a camera's sensor receives an intensity  $I_r$  and creates an image with a grayscale value of  $g_t$  then the relationship can be defined through Equation (5):

$$g_t = [G \cdot I_r + C]^\gamma \quad (5)$$

Where  $G$  is the gain,  $C$  the offset and  $\gamma$  the non-linearity co-efficient of the sensor. Assuming that the received intensity is equal to the emitted intensity a final expression can be obtained in Equation (6):

$$g_t = [G\Phi I_o(1 - e^{-C_{UV} \cdot x \cdot \varepsilon_\lambda}) + C]^\gamma \quad (6)$$

Where  $G\Phi I_o$  is typically replaced with a parameter  $A$  and  $C_{UV} \cdot \varepsilon_\lambda$  is replaced with a parameter  $B$ . This derivation demonstrates that it is feasible to extract fluid depths from grayscale intensities. In practical applications the build-up of contamination occurs via the deposition of droplets. As they accumulate they may become a film in some locations while remaining as discrete droplets in other.

Aguinaga & Bouchet's [14] work applies such a thin-film technique to the side glass of a car. Zones are defined to assess visibility through films of fluid. A threshold fluid depth is identified above which visibility is impacted. As such, the identification of fluid depths isn't fully utilised; a threshold intensity could just as easily have been identified. Furthermore, there is no distinction between a film and a droplet or rivulet when quantifying the visibility impact. This work will attempt to identify the volume of individual parcels of fluid and will consider differences between thin films and droplets.

The method described in this paper considers variations of illumination intensity coupled with a calibration vessel to initially study known droplets before being applied to a simplified contamination experiment with validated results for the total mass of fluid. If this method were applied to a contamination test with known spray duration, such as Kabanovs [11], then average contamination rates can be obtained with full spatial information so that validation of the CFD and detailed analysis of the contamination can be performed.

## Experimental Methodology

To develop the methodology experiments are conducted whereby droplets of doped water are created on a surface. They are illuminated with a UV light source and a calibration vessel is included within the image. High resolution images are taken that capture both droplet and calibration vessel (as shown in Figure 5). The emitted intensity from the calibration vessel is used to calculate the depth of fluid in the droplet.

## Experimental Arrangement

An experiment is setup such that UV dye doped droplets at 20, 40 and 60  $\mu\text{L}$  using a 1 ml syringe are created on a matt black vinyl surface. This choice of surface will minimise any reflection effects that may be present if a reflective material, such as painted aluminium, is used. A calibration vessel is placed in every frame to provide a controlled baseline of known fluid depth and resulting intensity such that an intensity anywhere else in the image can be converted back to a depth. The vessel has a flat plate (covered in the same matt black vinyl) that is machined with a slight incline such that the height decreases linearly by 0.83 mm over a 50 mm distance as show schematically in Figure 4.

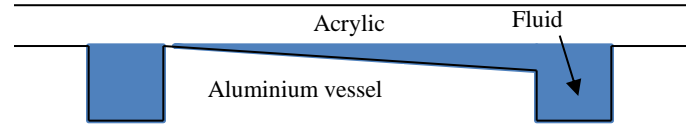


Figure 4. Schematic showing side section view of calibration vessel. Slope is 0.83mm over 50mm length

This vessel is filled with doped water (Uvitex NFW at 0.03 % concentration) and sealed with an acrylic lid to allow the vessel to be oriented as required. When illuminated by UV light that has a peak wavelength at 365 nm the dye emits a blue light with a typical wavelength of 475 nm. The low concentration of Uvitex ensures that the fluid's density can be assumed to be that of the de-ionised water. De-ionised water is used to ensure no chemical reaction with the salts typically found in tap water. Photobleaching effects are minimised by ensuring the same fluid is used for the droplets and vessel and both are exposed for minimal time.

The calibration vessel is located adjacent to the droplet and a plan image is captured with a sensor to surface distance of 622 mm using a DSLR with a 100 mm macro lens and exposure settings of ISO800, f/8, 1/80 s. The side profile is taken simultaneously with a separate DSLR using a 180 mm macro lens. Figure 5 shows the side profile camera at the bottom of the picture and the calibration vessel top left, the camera for acquiring the plan view image is out of shot.

The exposure settings were controlled to produce a near black image without illumination and an unsaturated image with the largest droplet illuminated. To further reduce unwanted reflections an image was captured on both cameras prior to the placement of the droplet on the test surface. During processing this image was then subtracted from the image of the droplet, resulting in an image containing just the droplet.

The image (Figure 5) also shows a metal ruler that was used for both focusing the plan view camera and obtaining spatial resolutions. During testing the region covered by the left hand side of the ruler was covered with the vinyl. Both side and plan cameras have a suitable spatial calibration of approximately 250 pixels per millimetre (ppmm) and 38 ppmm respectively.

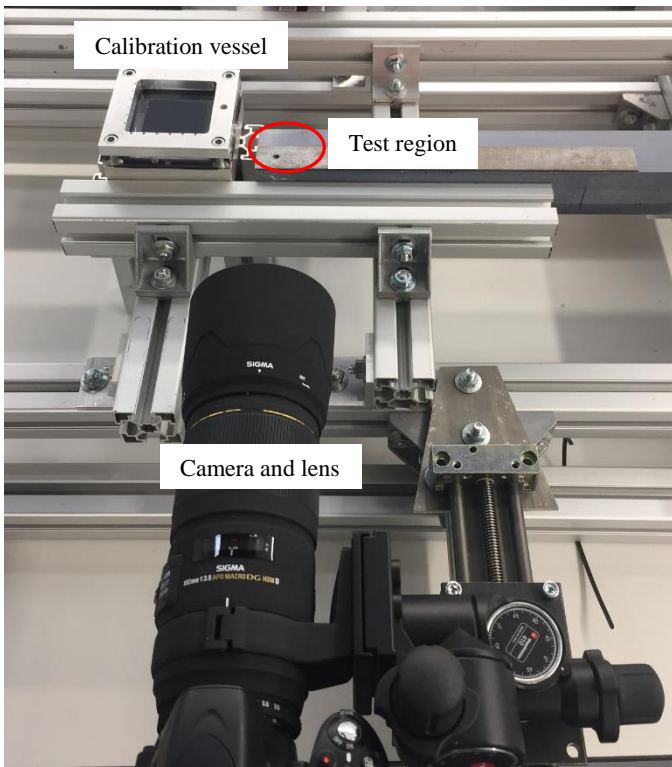


Figure 5. Experimental arrangement (minus UV lamp and plan camera)

The side images capture the emitted light from the droplet, which is binarised to allow a side-profile of radius against height to be identified. The spatial calibration taken at the start of the experiment is used to convert the image into millimeters. These provide a second known depth of fluid but for a droplet rather than a film such as in the calibration vessel. All images are taken in the camera's own RAW file format to ensure no processing of data is performed by the camera. These are loaded into MATLAB ready for processing. The resulting images are shown in Figure 6.

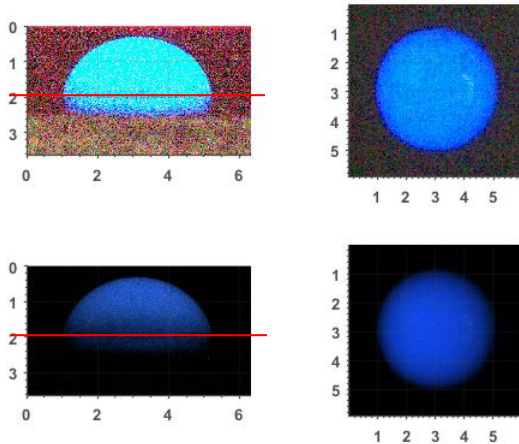


Figure 6. Example droplet imagery. From top left, clockwise: side image as taken, plan image as taken, plan image blue channel with background subtract, side image blue channel with background subtract (dimensions in mm).

The benefits of the background subtract are clearly seen in that they produce a zero value for everywhere that is not the droplet. When the grayscale value is converted back to a depth background noise will

not contribute to the calculated mass. The reflection of the hydrophilic droplet is visible on the side profiles, with the surface location shown by the red line. However, since these are only used to identify the geometry from the contact points they don't impact on the results.

## Processing Methodology

### Correcting for Incident Intensities and Absorption

When a typical contamination image is taken, the UV doped water on the surface is exposed directly to the UV light, whereas the doped water in the calibration vessel has a 10 mm thick piece of acrylic covering it. This is illustrated schematically in Figure 7; the exposed surface shown on the left and the acrylic covering the calibration vessel on the right. The acrylic will attenuate both the UV light entering the vessel (transmissivity  $\tau_{365}$ ) and the blue, emitted light, exiting it (transmissivity  $\tau_{475}$ ).

Aguinaga's derivation of the relationship between the camera's grayscale value,  $g_t$ , and the thickness of the fluid,  $x$ , can be adjusted to account for the presence of an acrylic block. Recalling Equation (4):

$$I_f = \Phi I_o (1 - e^{-C_{UV} \cdot x \cdot \epsilon_\lambda}) \quad (7)$$

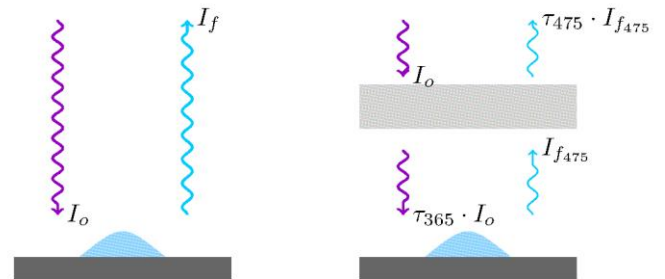


Figure 7. Schematic showing the effect of acrylic on incident and emitted intensities

The incident intensity,  $I_o$ , through the acrylic block becomes  $\tau_{365} \cdot I_o$  and the received intensity at the camera's sensor,  $I_f$ , becomes  $\tau_{475} \cdot I_{f_{365}}$ . As such, the grayscale value previously defined in Equation (6) can be defined in Equation (8):

$$g_t = [G\tau_{475}\Phi\tau_{365}I_o(1 - e^{-B \cdot x}) + C]^\gamma \quad (8)$$

As described in the introduction,  $G\Phi I_o$  is typically replaced with a parameter  $A$ . However, since the illumination intensity varies across the image domain  $I_o$  must be included as a function of the location in calculations.

To compensate for the UV transmissivity effect the power with and without the acrylic was measured using a power meter and the transmissivity calculated. The results are shown in Figure 8, with the powers shown in light and dark blue on the primary axis on the left:

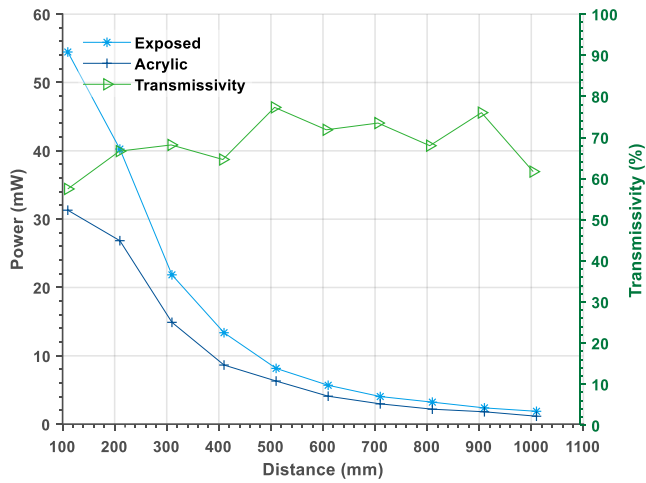


Figure 8. Attenuating effect of acrylic on UV power

The transmissivity ( $\tau_{365}$ ), shown in green and plotted on the secondary axis on the right, is typically 60-75 % independent of distance from the illumination source. This confirms available data for acrylic UV transmissivity ( $\tau_{365}$ ). The same data also gives the transmissivity for blue light ( $\tau_{475}$ ) as 98%.

The spatial variation of incident intensity,  $I_o$ , is quantified by taking an image of a blank sheet of white paper exposed and illuminated by the test conditions. The blue channel is then normalised by the peak value. The relative incident intensity for every pixel in a test image can be correctly identified, for example at the location of the droplet or calibration vessel.

Figure 9 shows the original calibration vessel data (uncorrected) for known fluid depth and recorded grayscale value with light blue stars. The base curve fit, i.e. Equation 6, to this data is shown by the dark blue line with triangular markers. The correction for incident intensity is shown by the light green line with circular markers and the correction for both the incident intensity and transmissivity is shown by the dark green line with diamond markers.

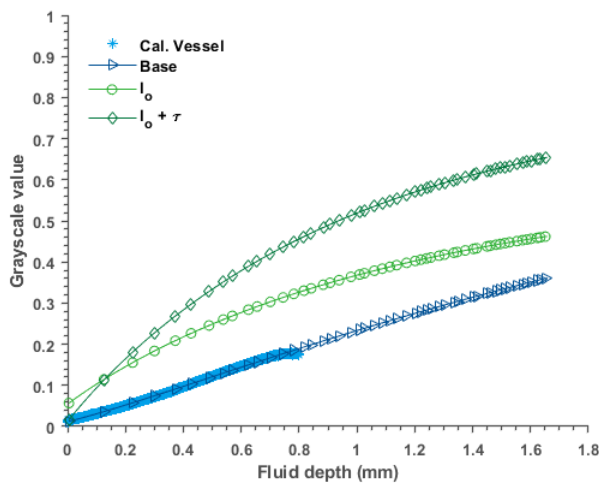


Figure 9. Normalised grayscale value against fluid depth for typical thin film approach

This final corrected curve fit is a complete calibration for the identification of thin films. However, since contamination

(especially base) is generally caused by spray the method should be examined for its suitability for application to a deposited spray.

### Droplet Corrections

To examine the suitability of the thin film base calibration technique two of the droplets, one of  $20 \mu L$  and the other  $40 \mu L$ , will be further processed. Since the droplets are within a known region of the image they can be identified using a circle finding algorithm (such as a circular Hough transformation [15]) applied to a binarised version of the image shown in Figure 6. The centre of the circle is used to turn the grayscale values from a cartesian co-ordinate system into a polar one, resulting in a profile like that shown in Figure 10. The radius is on the x-axis and the angle is on the y-axis with the colour indicating the normalised grayscale. The strange peaks from 2.3-3.3 mm are the corners of the image; the corners are further from the centre than the edges.

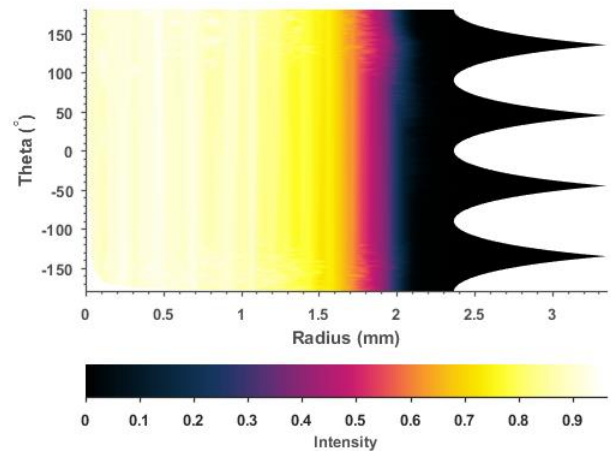


Figure 10. Normalised grayscale as a function of radius and angle for a typical droplet such as in Figure 6

The banded appearance along the radius is due to the high level of circularity for this droplet size. That is, the grayscale at any angle  $\theta$  from the centre is nearly constant for a fixed radius. The mean grayscale is then calculated along the radius, shown in Figure 11, resulting in  $g_t$  as a function of  $r$ .

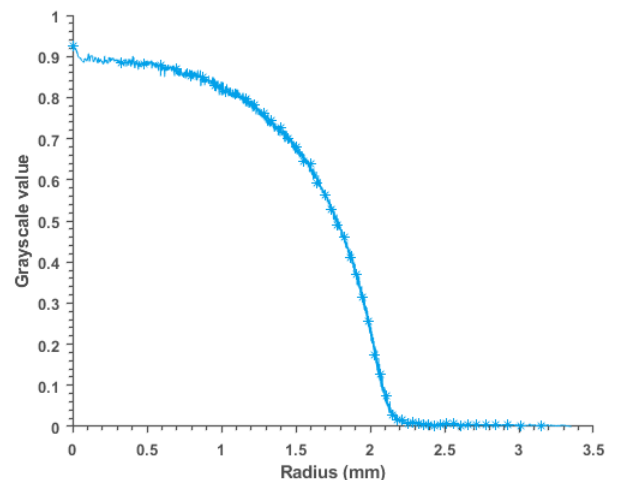


Figure 11. Example droplet radius (mm) against grayscale value

It is then possible to use the image from the side profile to determine the actual height at any radius. Figure 12 illustrates this, again assuming axial symmetry. The combination of these two data sets ( $r$  vs  $g_t$  and  $r$  vs height) means it is feasible to obtain the grayscale at any given height. The  $60 \mu\text{L}$  droplets showed reduced circularity and hence the assumptions about axial symmetry became invalid and the data was not used.

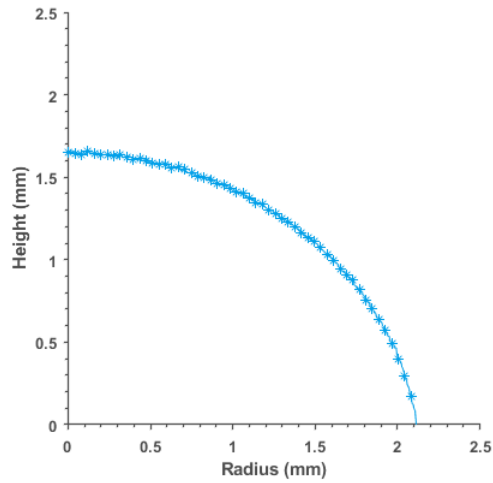


Figure 12. Example droplet radius (mm) against height (mm)

The example data shown in Figure 11 and Figure 12 are then plotted alongside the corrected thin film calibrations (shown in Figure 9) in Figure 13. The example droplet is shown by the gray plus symbols. The graph shows that the thin film calibration would underpredict the depth of fluid for depths below 0.65 mm and overpredict above, showing that there are some physical phenomena, such as refraction, to be considered. However, a simple empirical approach of fitting a quadratic correction factor models the curve adequately and the effectiveness is seen later. The three parameters are fitted using the actual height and intensity data from one  $20 \mu\text{L}$  and one  $40 \mu\text{L}$  droplet and are shown by the orange line. The corrections show a change in the profile of the curve that would significantly alter any estimates of depth.

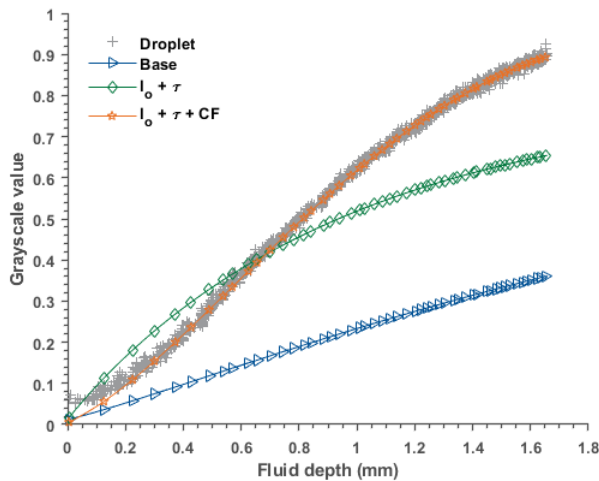


Figure 13. Normalised grayscale value against fluid depth; calibration fit (Base), thin film fit ( $I_0 + \tau$ ) and actual droplet data ( $I_0 + \tau + CF$ )

## Identifying Mass of Fluid

Tightly cropped images of the droplets can be turned from a grayscale to an estimated fluid depth at every location using the corrected data shown by the orange line in Figure 13. These heights are multiplied by the square of the spatial resolution to result in a volume at every location. This volume is summed to give a total volume before multiplying by the density to give a total mass.

As the droplets for the calibration were manually created using a 1 ml syringe with  $20 \mu\text{L}$  markings a separate test was conducted using the same syringe to create numerous droplets with target volumes of 20, 40 and  $60 \mu\text{L}$  on a set of scales accurate to 1 mg. The standard deviation and mean of these weighed drops is used to plot the known droplet volume on the x-axis of Figure 14.

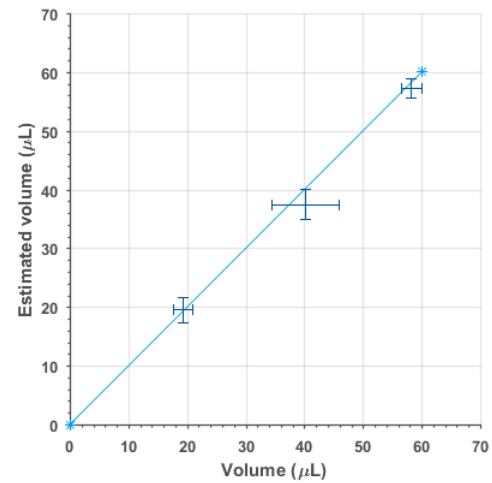


Figure 14. Actual vs estimated volumes of droplets using the corrected curve fit

The mean and standard deviation of the estimated volumes from the imaging tests are shown on the y-axis (estimated volume). A light blue line is drawn through equal volumes for reference. Figure 14 demonstrates that the method identified volumes accurately, typically within  $2 \mu\text{L}$  or between 3 and 10 %, at all three tested volumes, suggesting its suitability for applications where large droplets are not expected (large droplets risk moving and therefore destroying location data in the contamination test) and the image is sufficiently high in resolution to capture the grayscale gradient.

## Application to Contamination Type Tests

To demonstrate the suitability of the refined process, a second experiment is configured similar to that described previously. In this case no side image is captured and rather than a single volume droplet being created an uncharacterised spray is formed over a vinyl covered surface mounted on a set of scales resulting in a collection of differently sized drops and the potential for the droplets to coalesce in places to form a local film. The amount of spray was built up progressively and after every application the mass is noted and a plan image is captured. The same exposure settings are used as before but at a distance of 910 mm from the test surface to give a field of view that contains both the sprayed region and the calibration vessel. Three sprays are performed to incrementally increase the volume of fluid on the surface and change the location and structure of the drops. The complete process is repeated five times.

A spatial calibration of 21 ppm is achieved and the relative incident intensity in the region of interest is typically 67 %. As before, the calibration data is extracted from the image and a curve fit, including the transmissivities and incident intensity variation, obtained as shown in Figure 15. As previously observed, the corrections make a significant difference to the curve fits. The images are processed to obtain the depth of fluid at every pixel for every curve fit shown in Figure 15 and then summed to obtain the total mass of fluid for the region of interest.

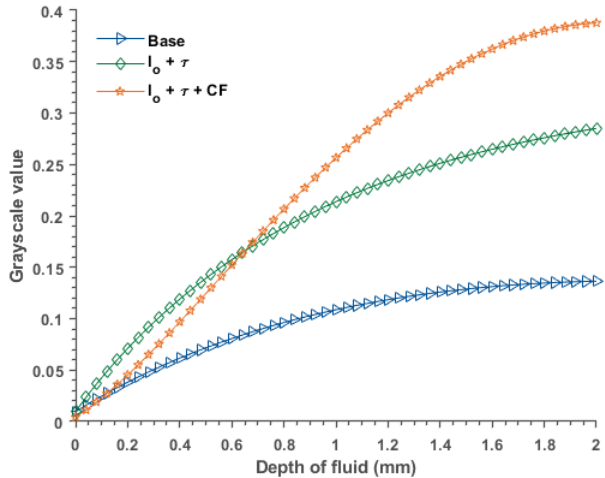


Figure 15. Calibration data for sprayed surface tests; calibration fit (Base), thin film fit ( $I_o + \tau$ ) and corrected thin film fit ( $I_o + \tau + CF$ )

Figure 16 shows the measured mass against the estimated mass for all the sample points in all the tests. The red line is a reference target line and the points are colour coded to match the curve fits in Figure 15. It is apparent that there is a spread of data across the calibration methods with the closest match being the thin film calibration with the intensity and absorption considered. The additional correction factor performs well with the smaller masses but overestimates at the larger masses. This may be a result of the increased range of grayscale values that can be resolved (0-0.4) compared to the  $I_o + \tau$  fit that can only resolve 0-0.3. If a grayscale value is higher than the curve fit then the depth of fluid is set to zero to stop any undesirable extrapolation. Further, the reduced spatial resolution compared to the first test may result in a shift towards all fluid appearing as a thin film. Additionally, the higher measured masses tended to have a large pool of fluid present. The implication is that there is a shift from a calibration that is corrected for droplets (demonstrated earlier in the work) to a more typical thin film calibration (with corrections for incident intensity). Taken to extremes the surface has either a single droplet on it or a significant quantity such that it is a thin film.

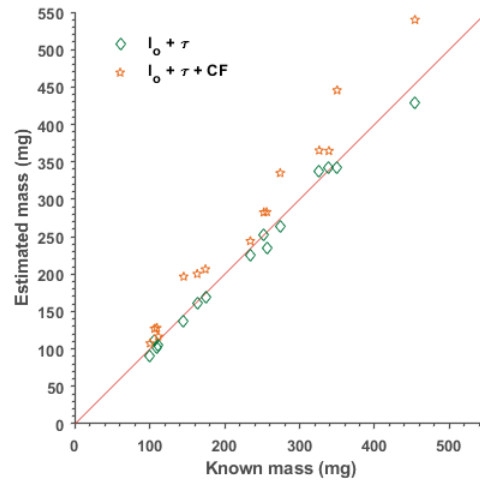


Figure 16. Actual vs estimated mass via different calibrations

Figure 17 shows a contour map of the data, with two lines drawn (one in blue and the other in green) that are then shown in profile in Figure 18. There is some fine spray ( $radius < 0.4mm$ ) that has been resolved along with larger pools of fluid. There are some misleading spots of zero data in the centre of a few of these pools (labelled **A**). Inspecting the original images reveals that these are collections of very small air bubbles in the fluid caused by the nature of the spray generation. Such bubbles are unlikely to occur in typical automotive contamination. These bubbles produce a high grayscale level around their circumference, likely due to a combination of refraction and potentially internal reflection, with a very low grayscale value inside the bubble. When processed these high values fall out of the range of expected intensity and are hence set to zero. This will impact on the estimated volume in that region; since this is the highest point of the fluid the estimated volume will under-predict the actual value.

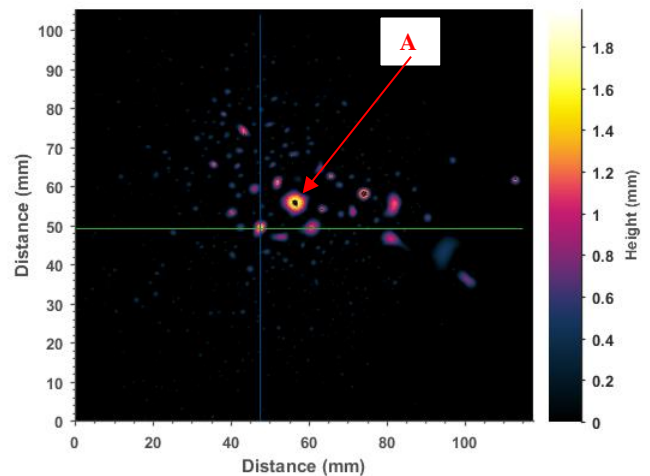


Figure 17. Contour of tested surface showing fluid depth. Green and blue lines are shown in profile in Figure 18

The impact on the estimate of height of the air bubbles can be clearly seen in the bottom x-axis of Figure 17 at around 50 mm. The estimated height drops from nearly 1.8 mm to zero and then back. The larger zero area (**A**) is approximately 1 mm<sup>2</sup> and again around 1.8 mm deep, equating to 1.8 mg. As such, although these regions are clearly apparent they do not represent significant errors.

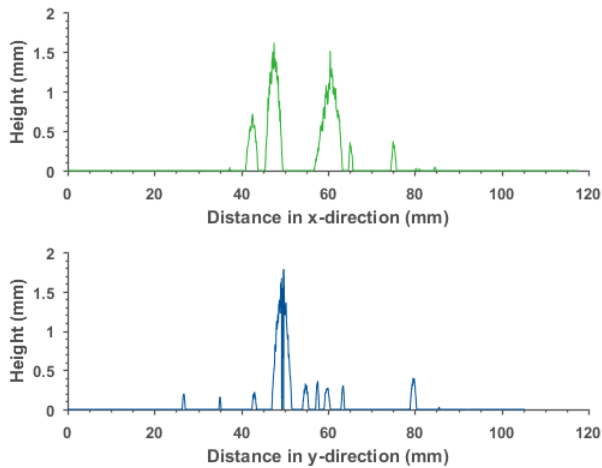


Figure 18. Example profiles from contour (colour matched for clarity)

Figure 19 explains this effect more clearly. It shows a cumulative distribution histogram of the non-zero depths of fluid from the data shown in the contour plot in Figure 17. The population below 1.7 mm, that is the depth of fluid in the region A, is 99.8%. As such, the majority of the total mass arises from smaller depths of fluid. This issue would have greater impact should that pool of fluid fall into a specific region of interest, at which point it would be a much larger percentage of the population.

It can be seen that approximately 95 % of the pixel population has a depth of fluid less than 1 mm. Referring back to Figure 15 it can be said that there is some offsetting in the 0-1 mm range between the fully corrected calibration data and the  $I_o \cdot \tau$  corrected data. For example 85% of the population is below the crossover at 0.6 mm where the corrected calibration curve results in a higher depth for a given grayscale. This may give an indication as to why the  $I_o \cdot \tau$  corrected data has the best result.

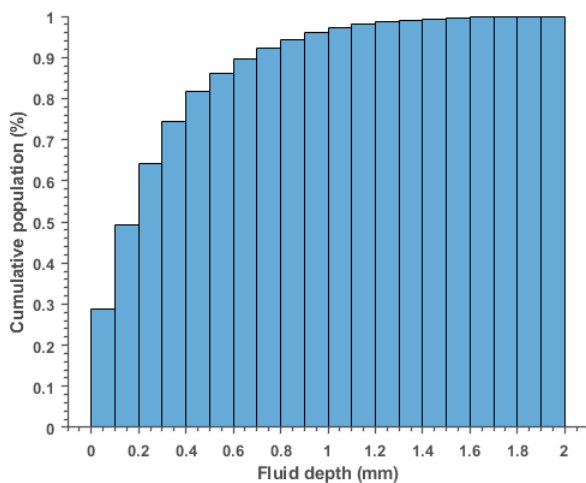


Figure 19. Histogram showing cumulative population of fluid depths for Figure 18

## Summary/Conclusions

This paper presents a methodology that can turn a grayscale intensity image typically taken during contamination tests into an objective

measure. This measure can then be used to determine average rates of contamination in regions of interest.

Experiments were conducted to understand the spatial lighting variations that may exist in contamination tests. These variations have been quantified and used to correct the results obtained.

The key parameters to be considered are identified and their application demonstrated. Discrepancies resulting from large droplets at high resolutions are resolved through an empirical process.

Controlled surface contamination experiments have been undertaken using a simplified approach. The methodology developed estimates the fluid mass typically within 8% of the actual mass for single droplets and within 10% for a sprayed surface using the corrected thin film approach. The method will allow for the study of specific regions of interest within an image, for instance the glass or camera location in base contamination tests.

This measure provides a foundation to perform quantitative comparisons between experiment and CFD, to quantify the benefits of vehicle configuration changes, and to study any variances between test sessions.

Further work should be undertaken to examine any difference in expected depth of fluid in the calibration vessel to actual depth. The calibration vessel should also be redesigned to give a greater range of depths, removing the requirement to extrapolate curve fits. Although the initial method demonstrated that the approach can be applied to a droplet further consideration around refraction issues is required, as is the potential for air bubbles to invalidate the process. Due consideration of further optical problems such as reflection from a surface such as metal is also required. The potential for a shifting calibration dependent on some function of the pool of fluid itself is also worthy of consideration.

The imaging arrangements used in this work can be applied to video footage of contamination tests. This would provide time resolved contamination data. However, there are some significant experimental issues that require resolving prior to being able to apply the techniques demonstrated here. Cameras would have to be placed in the tunnel environment and so a method for keeping the lens clear would be required. Furthermore, any spray in the air between the camera and the base would be illuminated resulting in a false intensity in the camera. Even if the light source were a vertical sheet aligned with the base then the presence of large fluid particles between the camera and the base would obscure the base and thus the results.

Finally, this methodology needs applying to actual base contamination tests in a wind tunnel. Testing of any model configuration should be undertaken with different spray durations since it has been previously shown [11] that there are low frequency events that may alter the rate of contamination. The averaged deposition rates can then be compared to simulation work, finally providing sensible objective comparisons between the two.

## References

1. Hagemeier T., Hartmann M., and Thevenin D.. Practice of vehicle soiling investigations: A review. International Journal of Multiphase flow, 37(8):860-875,doi:10.1016/j.ijmultiphaseow.2011.05.00, 2011.

2. Kuthada, T. and Cyr, S. Approaches to Vehicle Soiling. Progress in Vehicle Aerodynamics, Numerical Methods., Renningen: Expert Verlag, vol. IV, pp. 111-123, 2006
3. G. Maycock. The problem of water thrown up by vehicles on wet roads. In Road Research Laboratory Report No.4, Harmondsworth, Harmondsworth, 1966.
4. Gaylard, A. P., Kirwan, K. and Lockerby, D. Surface Contamination of cars: A review. Proc. IMechE Part D: J Automobile Engineering (2017) Vol. 231(9) 1160-1176
5. Vollmer, H., Gau, H., Klussman, S. et al. Comparison of On-road and Wind Tunnel Testing of Side Window Soiling Using a New Method. Progress in Vehicle Aerodynamic and Thermal Management, 2015. 276-288.
6. A. P. Gaylard, J. Pitman, J. Jilesen, A. Gagliardi, B. Duncan, J. Wanderer, and A. Konstantinov. Insights into Rear Surface Contamination Using Simulation of Road Spray and Aerodynamics. SAE International J. Passeng. Cars - Mech. Syst., 7(2):673–681, doi:10.4271/2014–01–0610, 2014.
7. A. P. Gaylard and B. Duncan. Simulation of Rear Glass and Body Side Vehicle Soiling by Road Sprays. SAE International J. Passeng. Cars - Mech. Syst., 4(1):184–196, doi:10.4271/2011–01–0173, 2011.
8. J. Jilesen, A. Gaylard, B. Duncan, A. Konstantinov, and E. Al. Simulation of Rear and Body Side Vehicle Soiling by Road Sprays Using Transient Particle Tracking. SAE International J. Passeng. Cars - Mech. Syst., 6(1):424–435, doi: 10.4271/2013–01–1256, 2013.
9. Karbon, K. J. and Longman, S. E. ‘Automobile Exterior Water Flow Analysis using CFD and Wind Tunnel Visualization’. SAE International J. Passeng. Cars – Mech. Syst. 980035 (1998).
10. Kabanovs, A., Varney, M., Garmory, A., Passmore, M. et al., "Experimental and Computational Study of Vehicle Surface Contamination on a Generic Bluff Body," SAE Technical Paper 2016-01-1604, 2016, doi:10.4271/2016-01-1604.
11. Kabanovs, A., Hodgson, Garmory, A., Passmore, M. et al., “A Parametric Study of Automotive Rear End Geometries on Rear Soiling,” SAE Int. J. Passeng. Cars – Mech. Syst. 10(2):2017, doi:10.4271/2017-01-1511.
12. Aguinaga, S., Boree, J., Simonin, I. et al., “Droplets dispersion and deposition measurements in an axisymmetric sudden expansion flow”. 14<sup>th</sup> International Symposium on Applications of Laser Techniques to Fluid Mechanics, Lisbon, Portugal, 2008
13. Hagemeyer T., Hartmann, M., Kuhle, M., Thevenin, D., and Zahringer, K. ‘Experimental characterization of thin films, droplets and rivulets using LED fluorescence’. Exp. Fluids (2012) 52:361–374.
14. Aguinaga, S., Bouchet, J.P. Quantitative Assessment by UV Fluorescence of Rain Water Flow on Vehicle Body in the Jules Verne Climatic Wind Tunnel. Progress in Vehicle Aerodynamics and Thermal Management, pp. 127-142, 2009.
15. T.J Atherton, D.J. Kerbyson. "Size invariant circle detection." Image and Vision Computing. Volume 17, Number 11, 1999, pp. 795-803.

## Contact Information

G. Hodgson  
[g.hodgson@lboro.ac.uk](mailto:g.hodgson@lboro.ac.uk)

M. Passmore  
[m.passmore@lboro.ac.uk](mailto:m.passmore@lboro.ac.uk)

A. Garmory  
[a.garmory@lboro.ac.uk](mailto:a.garmory@lboro.ac.uk)

A. Gaylard  
[agaylar1@jaguarlandrover.com](mailto:agaylar1@jaguarlandrover.com)

## Acknowledgments

This work was supported by Jaguar Land Rover and the UK Engineering and Physical Sciences Research Council grant EP/K014102/1 as part of the jointly funded Programme for Simulation Innovation.